Biomedical Optics EXPRESS

Large-field high-speed polarization sensitive spectral domain OCT and its applications in ophthalmology

Stefan Zotter,[1*] Michael Pircher,[1] Teresa Torzicky,[1] Bernhard Baumann,[1] Hirofumi Yoshida,[3] Futoshi Hirose,[3] Philipp Roberts,[2] Markus Ritter,[2] Christopher Schütze,[2] Erich Götzinger,[1] Wolfgang Trasischker,[1] Clemens Vass,[3] Ursula Schmidt-Erfurth,[2] and Christoph K. Hitzenberger[1]

[1]*Center for Medical Physics and Biomedical Engineering, Medical University of Vienna, Währinger Gürtel 18-20, A-1090 Vienna, Austria*

[2]*Department of Ophthalmology and Optometry, Medical University of Vienna, Währinger Gürtel 18-20, A-1090 Vienna, Austria*

[3]*Canon Inc., Tokyo, Japan*

**stefan.zotter@meduniwien.ac.at*

Abstract: We present a novel spectral domain polarization sensitive OCT system (PS-OCT) that operates at an A-scan rate of 70 kHz and supports scan angles of up to 40° × 40°. The high-speed imaging allows the acquisition of up to 1024 × 250 A-scans per 3D scan, which, together with the large field of view, considerably increases the informative value of the images. To demonstrate the excellent performance of the new PS-OCT system, we imaged several healthy volunteers and patients with various diseases such as glaucoma, AMD, Stargardt's disease, and albinism. The results are compared with clinically established methods such as scanning laser polarimetry and autofluorescence.

OCIS codes: (170.0170) Medical optics and biotechnology; (170.0110) Imaging systems; (170.2655) Functional monitoring and imaging; (170.4470) Ophthalmology; (170.4500) Optical coherence tomography

References and links

1. D. Huang, E. A. Swanson, C. P. Lin, J. S. Schuman, W. G. Stinson, W. Chang, M. R. Hee, T. Flotte, K. Gregory, C. A. Puliafito, and J. G. Fujimoto, "Optical coherence tomography," Science **254**(5035), 1178–1181 (1991).
2. A. F. Fercher, W. Drexler, C. K. Hitzenberger, and T. Lasser, "Optical coherence tomography - principles and applications," Rep. Prog. Phys. **66**(2), 239–303 (2003).
3. W. Drexler and J. Fujimoto, *Optical Coherence Tomography: Technology and Applications* (Springer, Berlin, 2008).
4. W. Drexler and J. G. Fujimoto, "State-of-the-art retinal optical coherence tomography," Prog. Retin. Eye Res. **27**(1), 45–88 (2008).
5. M. R. Hee, D. Huang, E. A. Swanson, and J. G. Fujimoto, "Polarization-Sensitive Low-Coherence Reflectometer for Birefringence Characterization and Ranging," J. Opt. Soc. Am. B **9**(6), 903–908 (1992).
6. J. F. de Boer, T. E. Milner, M. J. C. van Gemert, and J. S. Nelson, "Two-dimensional birefringence imaging in biological tissue by polarization-sensitive optical coherence tomography," Opt. Lett. **22**(12), 934–936 (1997).
7. M. Pircher, C. K. Hitzenberger, and U. Schmidt-Erfurth, "Polarization sensitive optical coherence tomography in the human eye," Prog. Retin. Eye Res. **30**(6), 431–451 (2011).
8. R. N. Weinreb, A. W. Dreher, A. Coleman, H. Quigley, B. Shaw, and K. Reiter, "Histopathologic validation of Fourier-ellipsometry measurements of retinal nerve fiber layer thickness," Arch. Ophthalmol. **108**(4), 557–560 (1990).
9. B. Cense, T. C. Chen, B. H. Park, M. C. Pierce, and J. F. de Boer, "Thickness and birefringence of healthy retinal nerve fiber layer tissue measured with polarization-sensitive optical coherence tomography," Invest. Ophthalmol. Vis. Sci. **45**(8), 2606–2612 (2004).
10. M. Pircher, E. Götzinger, R. Leitgeb, H. Sattmann, O. Findl, and C. K. Hitzenberger, "Imaging of polarization properties of human retina in vivo with phase resolved transversal PS-OCT," Opt. Express **12**(24), 5940–5951 (2004).

#171147 - $15.00 USD Received 21 Jun 2012; revised 24 Sep 2012; accepted 1 Oct 2012; published 3 Oct 2012

11. H. B. Brink and G. J. van Blokland, "Birefringence of the human foveal area assessed in vivo with Mueller-matrix ellipsometry," J. Opt. Soc. Am. A **5**(1), 49–57 (1988).
12. M. Pircher, E. Götzinger, O. Findl, S. Michels, W. Geitzenauer, C. Leydolt, U. Schmidt-Erfurth, and C. K. Hitzenberger, "Human macula investigated in vivo with polarization-sensitive optical coherence tomography," Invest. Ophthalmol. Vis. Sci. **47**(12), 5487–5494 (2006).
13. B. Thylefors, A. D. Négrel, R. Pararajasegaram, and K. Y. Dadzie, "Global data on blindness," Bull. World Health Organ. **73**(1), 115–121 (1995).
14. H. A. Quigley, "Number of people with glaucoma worldwide," Br. J. Ophthalmol. **80**(5), 389–393 (1996).
15. A. W. Dreher, K. Reiter, and R. N. Weinreb, "Spatially resolved birefringence of the retinal nerve fiber layer assessed with a retinal laser ellipsometer," Appl. Opt. **31**(19), 3730–3735 (1992).
16. Q. Zhou, J. Reed, R. Betts, P. Trost, P. Lo, C. Wallace, R. Bienias, G. Li, R. Winnick, W. Papworth, and M. Sinai, "Detection of glaucomatous retinal nerve fiber layer damage by scanning laser polarimetry with variable corneal compensation," Proc. SPIE **4951**, 32–41 (2003).
17. B. Baumann, E. Götzinger, M. Pircher, H. Sattmann, C. Schütze, F. Schlanitz, C. Ahlers, U. Schmidt-Erfurth, and C. K. Hitzenberger, "Segmentation and quantification of retinal lesions in age-related macular degeneration using polarization-sensitive optical coherence tomography," J. Biomed. Opt. **15**(6), 061704 (2010).
18. S. Michels, M. Pircher, W. Geitzenauer, C. Simader, E. Götzinger, O. Findl, U. Schmidt-Erfurth, and C. K. Hitzenberger, "Value of polarisation-sensitive optical coherence tomography in diseases affecting the retinal pigment epithelium," Br. J. Ophthalmol. **92**(2), 204–209 (2008).
19. C. Ahlers, E. Götzinger, M. Pircher, I. Golbaz, F. Prager, C. Schütze, B. Baumann, C. K. Hitzenberger, and U. Schmidt-Erfurth, "Imaging of the retinal pigment epithelium in age-related macular degeneration using polarization-sensitive optical coherence tomography," Invest. Ophthalmol. Vis. Sci. **51**(4), 2149–2157 (2010).
20. E. Götzinger, B. Baumann, M. Pircher, and C. K. Hitzenberger, "Polarization maintaining fiber based ultra-high resolution spectral domain polarization sensitive optical coherence tomography," Opt. Express **17**(25), 22704–22717 (2009).
21. B. Baumann, E. Götzinger, M. Pircher, and C. K. Hitzenberger, "Single camera based spectral domain polarization sensitive optical coherence tomography," Opt. Express **15**(3), 1054–1063 (2007).
22. C. K. Hitzenberger, E. Goetzinger, M. Sticker, M. Pircher, and A. F. Fercher, "Measurement and imaging of birefringence and optic axis orientation by phase resolved polarization sensitive optical coherence tomography," Opt. Express **9**(13), 780–790 (2001).
23. E. Götzinger, M. Pircher, W. Geitzenauer, C. Ahlers, B. Baumann, S. Michels, U. Schmidt-Erfurth, and C. K. Hitzenberger, "Retinal pigment epithelium segmentation by polarization sensitive optical coherence tomography," Opt. Express **16**(21), 16410–16422 (2008).
24. M. Pircher, E. Götzinger, B. Baumann, and C. K. Hitzenberger, "Corneal birefringence compensation for polarization sensitive optical coherence tomography of the human retina," J. Biomed. Opt. **12**(4), 041210 (2007).
25. E. Götzinger, M. Pircher, B. Baumann, C. Hirn, C. Vass, and C. K. Hitzenberger, "Retinal nerve fiber layer birefringence evaluated with polarization sensitive spectral domain OCT and scanning laser polarimetry: a comparison," J Biophotonics **1**(2), 129–139 (2008).
26. B. Cense, T. C. Chen, B. H. Park, M. C. Pierce, and J. F. de Boer, "Invivo depth-resolved birefringence measurements of the human retinal nerve fiber layer by polarization-sensitive optical coherence tomography," Opt. Lett. **27**(18), 1610–1612 (2002).
27. E. Götzinger, M. Pircher, B. Baumann, T. Schmoll, H. Sattmann, R. A. Leitgeb, and C. K. Hitzenberger, "Speckle noise reduction in high speed polarization sensitive spectral domain optical coherence tomography," Opt. Express **19**(15), 14568–14585 (2011).
28. T. Torzicky, M. Pircher, S. Zotter, M. Bonesi, E. Götzinger, and C. K. Hitzenberger, "Automated measurement of choroidal thickness in the human eye by polarization sensitive optical coherence tomography," Opt. Express **20**(7), 7564–7574 (2012).
29. M. Mujat, B. H. Park, B. Cense, T. C. Chen, and J. F. de Boer, "Autocalibration of spectral-domain optical coherence tomography spectrometers for in vivo quantitative retinal nerve fiber layer birefringence determination," J. Biomed. Opt. **12**(4), 041205 (2007).
30. M. Yamanari, M. Miura, S. Makita, T. Yatagai, and Y. Yasuno, "Phase retardation measurement of retinal nerve fiber layer by polarization-sensitive spectral-domain optical coherence tomography and scanning laser polarimetry," J. Biomed. Opt. **13**(1), 014013 (2008).
31. F. A. Medeiros, G. Vizzeri, L. M. Zangwill, L. M. Alencar, P. A. Sample, and R. N. Weinreb, "Comparison of retinal nerve fiber layer and optic disc imaging for diagnosing glaucoma in patients suspected of having the disease," Ophthalmology **115**(8), 1340–1346 (2008).
32. J. Choi, H. S. Cho, C. H. Lee, and M. S. Kook, "Scanning laser polarimetry with variable corneal compensation in the area of apparently normal hemifield in eyes with normal-tension glaucoma," Ophthalmology **113**(11), 1954–1960 (2006).
33. A. Kanamori, A. Nagai-Kusuhara, M. F. Escaño, H. Maeda, M. Nakamura, and A. Negi, "Comparison of confocal scanning laser ophthalmoscopy, scanning laser polarimetry and optical coherence tomography to discriminate ocular hypertension and glaucoma at an early stage," Graefes Arch. Clin. Exp. Ophthalmol. **244**(1), 58–68 (2006).

#171147 - $15.00 USD Received 21 Jun 2012; revised 24 Sep 2012; accepted 1 Oct 2012; published 3 Oct 2012

34. F. G. Schlanitz, B. Baumann, T. Spalek, C. Schütze, C. Ahlers, M. Pircher, E. Götzinger, C. K. Hitzenberger, and U. Schmidt-Erfurth, "Performance of automated drusen detection by polarization-sensitive optical coherence tomography," Invest. Ophthalmol. Vis. Sci. **52**(7), 4571–4579 (2011).

1. Introduction

Since its first introduction in the 1990s [1] OCT has developed into a powerful noninvasive imaging technique that provides high resolution, cross sectional images of translucent tissues [2,3]. In the meantime OCT has found a variety of applications in different fields such as neurology, dermatology, gastro-intestinal imaging and cardiology. Nevertheless it still has its main application in the field of ophthalmology [4]. Since 1992 a functional extension of conventional intensity based OCT called polarization sensitive OCT (PS-OCT) has been developed [5–7]. PS-OCT enables the differentiation of several layers within the retina due to the different light-tissue interaction mechanisms. The retinal layers can be categorized into polarization preserving layers (e.g. photoreceptor layer), birefringent layers (e.g. retinal nerve fiber layer (RNFL) or Henle's fiber layer) [8–11] and depolarizing (polarization scrambling) layers (e.g. retinal pigment epithelium (RPE)) [10,12]. PS-OCT is not only capable to distinguish these layers, which is important for segmentation, but it can also retrieve quantitative information about different structures within the retina.

One example for this is the ability of PS-OCT to measure the birefringence of the RNFL. This is especially interesting for diagnosis of glaucoma, one of the leading causes of blindness in the world [13,14]. During the progression of the disease ganglion cell axons within the RNFL degenerate which leads to a thinning of the RNFL and finally to visual field defects and blindness. One clinically established method for glaucoma diagnosis is scanning laser polarimetry (SLP) [15,16] such as the GDx VCC and ECC from Carl Zeis Meditec, which measures the circumpapillary retardation distribution caused by the RNFL, from which the status of the RNFL is derived. In comparison with SLP, PS-OCT has the fundamental advantage that it combines the ability of intensity based OCT to provide cross sectional images of the retina, giving direct access to the thickness of the RNFL, with the polarization sensitivity of SLP. With PS-OCT, RNFL thickness and retardation can be measured simultaneously but independently, providing access to the birefringence, the quotient of the two quantities. SLP measures only the retardation, which is a combined effect of thickness and birefringence.

The ability of PS-OCT to provide tissue specific contrast is also important in other diseases such as age related macular degeneration (AMD). AMD is another leading cause of visual loss and blindness. At an early stage of the disease, accumulations of extracellular material build up in Bruch's membrane. These deposits lead to an irregular RPE shape and detachments, which are called drusen. At an advanced stage of the disease, AMD can be classified into wet or dry AMD. The wet form of AMD is characterized by abnormal vessel growth in the choroid (choroidal neovascularization), which leads to subretinal fluids, RPE detachments, hard exudates, bleeding and scaring of tissue. The dry form of AMD is characterized by geographic atrophies (GA), areas with absence of RPE. The RPE plays a key role in all forms of AMD. Based on the depolarization effect of the RPE, PS-OCT can reliably segment and identify the RPE layer, which makes PS-OCT a valuable tool for AMD diagnosis [12,17–19].

In this paper we present a novel high-speed, large-field PS-OCT system. In contrast to previous PS-OCT systems [17,20], the new PS-OCT system supports a denser sampling (up to 1024 × 250 A-scans) over a larger scan field (up to 40° × 40°), which increases the explanatory power of the recorded images. Several healthy subjects and patients diagnosed with a variety of diseases, such as glaucoma, AMD, Stargardt's disease and albinism have been imaged with the new PS-OCT system. The high quality of the measurement results demonstrate that the novel PS-OCT system is able to combine the abilities of clinically established imaging methods, such as SLP and conventional intensity based OCT.

#171147 - $15.00 USD Received 21 Jun 2012; revised 24 Sep 2012; accepted 1 Oct 2012; published 3 Oct 2012

Furthermore, the new PS-OCT system is capable of providing specific information on the RPE layer as autofluorescence imaging. This is achieved due to the variety of information, which is acquired during a single measurement, combined with several additional post-processing steps.

2. Methods

2.1. Polarization sensitive OCT instrument

A schematic diagram of the novel PS-OCT is presented in Fig. 1. The system is based on a Michelson interferometer incorporating polarization maintaining (PM) fibers similar to the system described in [20]. Light from a superluminescent diode (center wavelength 836 nm, FWHM 54 nm) is coupled into a PM fiber polarizer. A polarization control paddle is inserted beforehand to match the polarization state with the orientation of the PM fiber polarizer. Afterwards the light is split into sample and reference arm at a 90:10 PM fiber beam splitter.

In the reference arm the light passes a quarter wave plate (QWP) oriented at 22.5°, a prism pair, which is used to compensate the dispersion mismatch between sample and reference arm and is reflected by a mirror which is mounted on a motorized stage to control the coherence gate position. An additional lens is mounted in front of the mirror, which introduces a defocus depending on the distance between the lens and the mirror. This defocus is used to adjust the reference arm power at the spectrometer. After double-passing the QWP the polarization state of the light is orientated at 45°. This configuration provides equal reference arm power for both channels of the polarization sensitive detection.

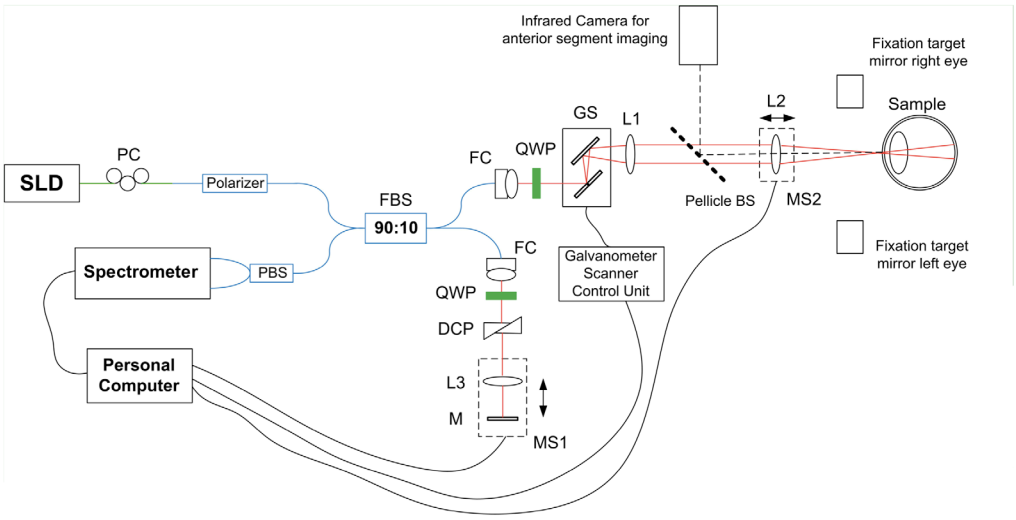

Fig. 1. Schematic diagram of the PS-OCT system. SLD, superluminescent diode; PC, polarization controller; FBS, fiber nonpolarizing beam splitter; PBS, fiber polarizing beam splitter; FC, fiber collimator; QWP, quarter-wave plate; DCP, dispersion compensating prism pair; L1-L3, lens; MS1-2, motorized stage; GS, galvanometer scanner; M, mirror; Pellicle BS, pellicle beam splitter; green lines, single mode fiber; red lines, free space beam path; blue lines, polarization maintaining fiber; black lines, cable connection.

In the sample arm light passes a QWP oriented at 45° to provide circular polarized light onto the eye. An x-y galvanometer scanner and a telescope consisting of an 80 mm (L1) and a 50 mm (L2) achromatic lens is used to scan the beam over the retina. The second telescope lens is mounted on a motorized stage to compensate for refractive errors of the patient. Additionally, a pellicle beam splitter can be flipped into the sample arm, which, in combination with an infrared camera, can be used as an anterior segment monitor. This anterior segment monitor is used to align the patient's head and the pellicle beam splitter is

#171147 - $15.00 USD Received 21 Jun 2012; revised 24 Sep 2012; accepted 1 Oct 2012; published 3 Oct 2012

removed prior to the measurement. As a fixation target we display a colored cross on a computer monitor, which is mounted on top of the sample arm unit. Two mirrors beside the last telescope lens allow the patient to see this fixation target with the eye that is currently not measured by the PS-OCT.

Light returning from the sample and reference arm interferes at the beam splitter and is afterwards split into two orthogonal polarization channels by a PM fiber based polarizing beam splitter. The two polarization channels are guided to a spectrometer. Contrary to the setup described in [20] where two individual spectrometers with two line scan cameras are used, the new PS-OCT system uses only a single line scan camera [21]. This configuration has the advantage of significantly reduced system costs and complexity, however, it requires several additional post-processing steps which are described in [21].

With an A-scan rate of 70 kHz and a light power of 730 µW incident at the cornea we measured a maximum sensitivity of 98 dB close to the zero delay line. The sensitivity dropped to 90 dB at 1.8 mm imaging depth. The measured axial resolution of the system is 7.8 µm in air. Various scan patterns ranging from 512 × 125 A-scans up to 1024 × 250 A-scans are available. However, for the results presented in this paper we used only the 1024 × 250 A-scan pattern because we found this pattern provided the best image quality. The maximum scan field is 40° × 40°.

2.2. PS-OCT data analysis

Since the new PS-OCT system is based on a single line scan camera approach, a pixel-to-pixel correspondence of the two spectral interferograms, which is required for polarization sensitive imaging, can only be achieved by applying several additional post-processing steps. The reason for this is the following: due to the fact that both spectra illuminate the diffraction grating at different incident angles, the recorded spectra will be distorted with respect to each other and the spectral range is imaged onto a different number of line scan camera pixels. The first post-processing step is to split the two spectra into two subsets consisting of an equal number of camera pixels. Afterwards the recorded wavelength range of one spectrum is adjusted to match the wavelength range of the other spectrum. This is done by either squeezing or stretching one spectrum with respect to the other. Then the two subsets are overlaid and one spectrum is shifted along the pixels to assure that each wavelength component of the two spectra corresponds to the same pixel. In this way a pixel to pixel correspondence between the two polarization channels is achieved. A more detailed discussion of these post-processing steps can be found in [21]. Afterwards standard post-processing steps, such as subtraction of the mean spectrum and rescaling from λ to k-space and Fourier-Transformation are performed.

From the processed 3D data set, which contains amplitude and phase information of both polarization channels, we can calculate the intensity, retardation, optic axis orientation [22] and degree of polarization uniformity (DOPU) values [23]. The DOPU values allow us to quantify the amount of depolarizing material within the retina. For this purpose every pixel with a DOPU value lower than 0.75 is extracted.

These post-processing steps are carried out for each recorded data set. Depending on the pathology of the patients various different additional post-processing steps are performed, which are described below.

2.2.1. Glaucoma

With PS-OCT the polarization properties of the birefringent RNFL can be quantified. In order to observe this birefringence, which leads to a linear increased retardation with depth, we first need to compensate the 3D polarization sensitive data for the birefringence of the anterior segment. This is achieved by measuring the polarization state at the surface of the retina and using a software based correction algorithm [24].

#171147 - $15.00 USD Received 21 Jun 2012; revised 24 Sep 2012; accepted 1 Oct 2012; published 3 Oct 2012

Afterwards we generate 2D en face retardation maps from the 3D polarization sensitive data. For this purpose, light that has double passed the birefringent RNFL and is reflected from a polarization-preserving layer needs to be detected. Here we choose the signal from the inner/outer photoreceptor junction (IS/OS junction) and the end tips of photoreceptor (ETPR) because these layers have a high reflectivity. This high reflectivity is desirable because it reduces noise of the retardation values. In order to segment the IS/OS junction and ETPR we take advantage of the depolarization effect (polarization scrambling) of the RPE that can be observed with PS-OCT [23]. After the segmentation of the anterior border of the RPE we analyze every retardation value along each A-scan within a window of 80 µm anterior to the RPE (this window contains the IS/OS and ETPR layer). These values are plotted in a histogram and the peak of the histogram is regarded as the retardation value that is assigned to the respective transverse position of the 2D retardation en face maps [25]. Afterwards the en face maps are thresholded, based on the corresponding intensity values, to exclude areas with low signal quality (e.g. regions that are shaded by blood vessels).

The next post-processing step is to generate 2D en face RNFL thickness and birefringence maps. For this purpose we segment the RNFL thickness from the intensity images. Our algorithm relies on the fact that the RNFL has a higher reflectivity than the surrounding layers. First a combination of a bilateral and median filter is applied to smoothen the intensity image and hence reduce speckle noise. Afterwards the anterior border of the RNFL is detected by searching for the first pixel along each A-scan that is above a certain intensity threshold. The posterior border of the RNFL is segmented by searching for the first pixel below another intensity threshold starting from the anterior border of the RNFL. From the obtained values for the posterior border of the RNFL, outliers, which are located far away from neighboring values, are removed before fitting with a polynomial function (polynomial order: 3). Again an intensity threshold is applied to the final 2D en face RNFL thickness maps to exclude areas with low signal quality.

For calculating en face birefringence maps, we use an algorithm that was previously published by Cense et al. [9,26]. First, the retardation values within the segmented RNFL are plotted against depth. Secondly, these values are fitted by a linear regression and the slope of this fit is regarded as the birefringence value of the RNFL at this transverse position. By repeating this procedure for every A-scan within the 3D data set, 2D en face birefringence maps are generated. Note that in contrast to previous works no averaging is performed [25].

2.2.2. RPE related retinal diseases

The post-processing procedure for patients with RPE related retinal diseases depends on the form of the disease. In the case of drusen, pigment epithelial detachments (PED) or irregular RPE shapes we apply a segmentation algorithm that is similar to the one described in [17]. In short, the algorithm works as follows. First the lowest DOPU value within every A-scan is detected. This pixel is usually located in the center of the RPE layer. From the obtained positions of the depolarizing pixels, outliers, which are located far away from the neighboring segmented pixels, are removed and the obtained data points are fitted with an iterative Savitzky–Golay filter (filter length: 100 A-scans, polynomial order: 3) [17]. The result of this computation yields the approximated normal posterior position of the RPE (the posterior position where the RPE would be in the absence of drusen or PEDs). In the next step we first detect the anterior border of the RPE by searching for the first depolarizing pixel within every A-scan starting from the inner limiting membrane. The obtained values are again fitted with an iterative Savitzky-Golay filter (filter length: 6 A-scans, polynomial order 3). The result of this fit yields the actual anterior border position of the RPE. Drusen, RPE irregularities and PEDs can now be detected by calculating the difference between the estimated normal posterior position of the RPE and the actual anterior border. The values are recalculated to thickness, assuming a refractive index of 1.38. These RPE elevation maps allow us to quantify e.g. the number and size of drusen or the elevations of PEDs within the retina.

#171147 - $15.00 USD Received 21 Jun 2012; revised 24 Sep 2012; accepted 1 Oct 2012; published 3 Oct 2012

In order to detect atrophic zones in dry AMD we simply add the number of depolarizing pixels along each A-scan within the 3D PS-OCT data set. The resulting 2D en face map gives us information about the amount of depolarizing material within the retina. These maps reveal the area and size of geographic atrophies, which appear as sharp delineated areas with absent RPE. Again these maps are recalculated to thickness assuming a refractive index of 1.38.

The same post-processing algorithms can be applied to patients with Stargradt's disease.

3. Results—healthy eyes

Exemplary measurement results with the new high-speed, large-field PS-OCT system are presented in Fig. 2. Figure 2(A) shows the pseudo SLO image from a 3D PS-OCT data set recorded in a healthy human volunteer (scan pattern 1024 × 250, scan angle 40° × 40°). The yellow line indicates the position of the extracted B-scans (2(B) intensity, 2(C) retardation, 2(D) optic axis orientation, 2(E) DOPU, 2(F) segmented depolarizing material overlaid with the intensity image). Figures 2(B1), 2(E1) and 2(F1) show magnified areas of the RPE and

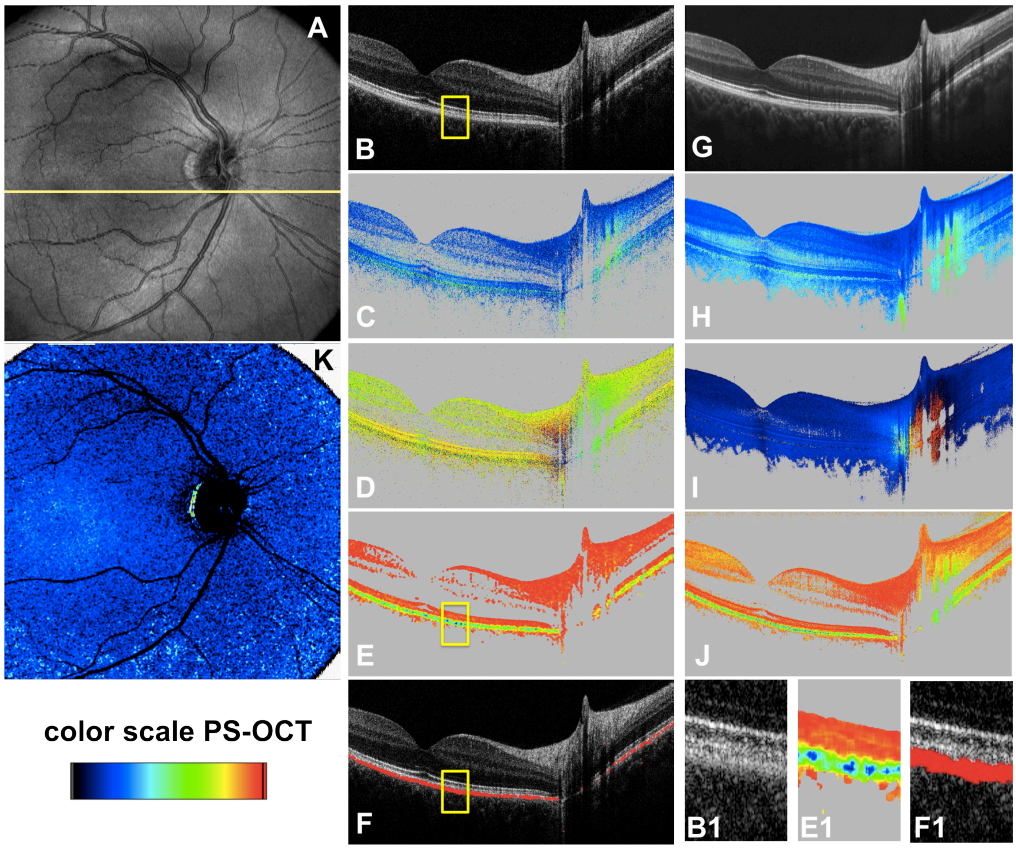

Fig. 2. Exemplary PS-OCT measurement results from a healthy human volunteer (scan angle: 40° × 40°, scan pattern 1024 × 250 A-scans). (A) Pseudo SLO, yellow line marks the location of the corresponding B-scans. (B) Intensity B-scan on logarithmic gray scale. Yellow box indicates area of the magnified image, B1. (C) Retardation image (color scale 0-90°). (D) Optic axis orientation (color scale 0-180°). (E) DOPU image (color scale 0-1). Yellow box indicates area of the magnified image, E1. (F) Segmented depolarizing material (red) overlaid with the intensity image. Yellow box indicates area of the magnified image, F1. (G) Average of 50 intensity B-scans recorded at the same position. (H) Average retardation image. (I) Average optic axis orientation image. (J) DOPU image calculated from a temporal window over 50 B-scans. (K) Depth summation of the number of depolarizing pixels along each A-scan within the 3D data set (color scale 0-100 µm). Areas with low signal quality are displayed in white.

#171147 - $15.00 USD Received 21 Jun 2012; revised 24 Sep 2012; accepted 1 Oct 2012; published 3 Oct 2012

photoreceptor layer extracted from the corresponding intensity (Fig. 2(B)), DOPU (2(E)) and RPE segmentation image (Fig. 2(F)). The area which is magnified is indicated by yellow boxes in the corresponding images. Figures 2(G)–2(I) show averaged intensity, retardation and optic axis orientation images. For these images, 50 B-scans, recorded at approximately the same position, were averaged using the same averaging procedure as in [27,28]. Figure 2(J) shows a DOPU image where a temporal window over 50 B-scans, instead of a spatial window (Fig. 2(E)), was used. Figure 2(K) shows a 2D depolarizing material en face map. For this image the amount of depolarizing material along each A-scan was added in depth. The image clearly shows the hyperpigmentation of the RPE in the foveal region. The brighter spots in the periphery, which can be seen at the edges of the image, are not due to stronger pigmentation in the RPE but they originate from a higher amount of depolarizing material in the choroid. In order to obtain a pure RPE thickness map one would need to exclude the signal from the choroid [17]. Nevertheless this type of image is very useful, especially in patients with geographic atrophies, as we will show later.

From the same data set 2D en face RNFL retardation, thickness and birefringence maps can be calculated. The results are presented in Fig. 3. The images show an increased RNFL retardation, thickness and birefringence in the superior and inferior region around the optic nerve head, which is in good agreement with previous findings [9,25,26,29,30]. With the new PS-OCT system very thin nerve fiber bundles and their distribution along the larger blood vessels within the retina can be observed. Noticeable is also the effect of Henle's fiber layer that generates a doughnut shape retardation pattern in the foveal region. The red rectangle in Figs. 3(B) and 3(C) indicate an area around the fovea where our RNFL thickness segmentation algorithm failed to segment the posterior border of the RNFL correctly. Blood vessels and areas with low signal quality are displayed in gray. Please note that in the birefringence map larger areas are excluded from the final image (gray values). Here we exclude areas where the RNFL thickness is below 60 µm because the birefringence cannot be calculated accurately.

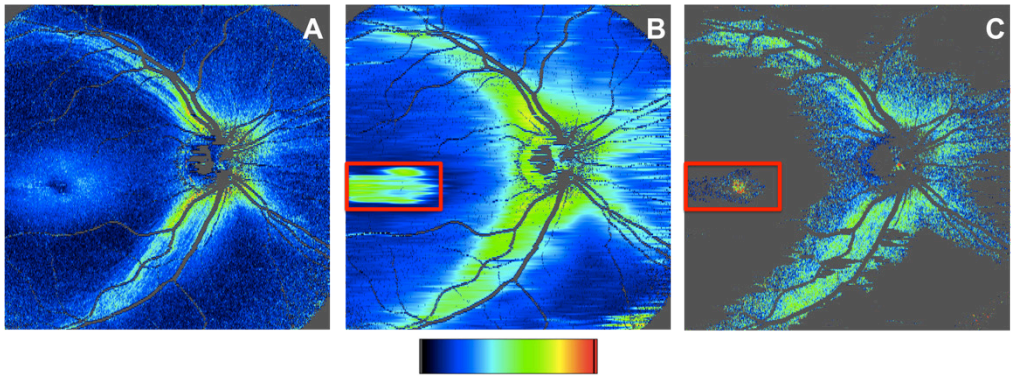

Fig. 3. 2D en face RNFL retardation (A) (color scale 0-50°), thickness (B) (color scale 0-200 µm) and birefringence (C) (color scale 0-0.3°/µm) maps calculated from the same data set presented in Fig. 2. Areas with low signal quality are displayed in gray. Additionally, in the birefringence en face map, areas with RNFL thickness bellow 60 µm are displayed in gray. Red rectangle in B and C indicates an artifact due to incorrect segmentation of the posterior border of the RNFL.

Figure 4 shows averaged RNFL retardation, thickness and birefringence images from another healthy volunteer. The volunteer was imaged five times with the PS-OCT system. For each obtained data set RNFL retardation, thickness and birefringence maps were calculated. The images were registered with respect to each other and averaged. Again, very thin nerve fiber bundles are clearly visible in the retardation and birefringence map. These fine details cannot be observed in the corresponding SLP measurement result (see Fig. 4(D)). The

#171147 - $15.00 USD Received 21 Jun 2012; revised 24 Sep 2012; accepted 1 Oct 2012; published 3 Oct 2012

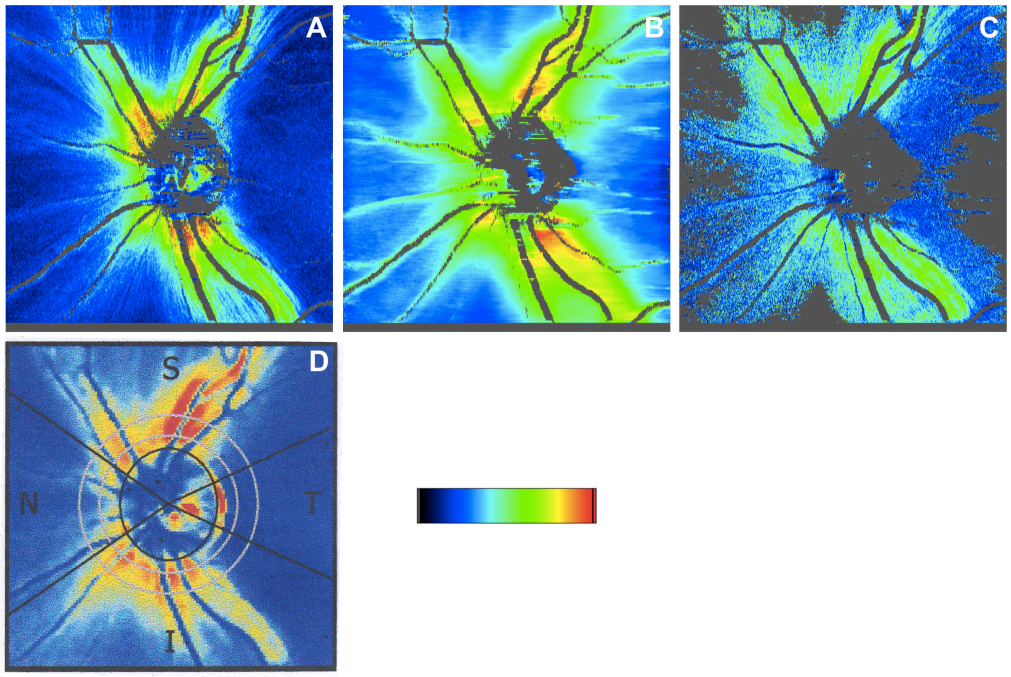

Fig. 4. Averaged RNFL retardation (A) (color scale 0-50°), thickness (B) (color scale 0-200 µm) and birefringence (C) (color scale 0-0.3°/µm) en face map, calculated for 5 repeated measurements recorded in the same eye of a healthy human volunteer. Scan protocol for each individual measurement: 1024 × 250 A-scans, scan angle 27° × 24°. Areas with low signal quality are display in gray. Additionally, in the birefringence en face map, areas with RNFL thickness below 60 µm are displayed in gray. (D) Retardation measured by SLP (GDx VCC) in the same subject.

birefringence map further shows that the birefringence is not constant throughout the RNFL. Instead a clear increase of RNFL birefringence can be observed in the superior and inferior region around the optic nerve head [25,29,30].

4. Results - diseased eyes

4.1. Glaucoma suspect

An exemplary measurement result for a glaucoma suspect patient can be seen in Fig. 5. The en face retardation image clearly shows a reduced RNFL retardation and hence nerve fiber

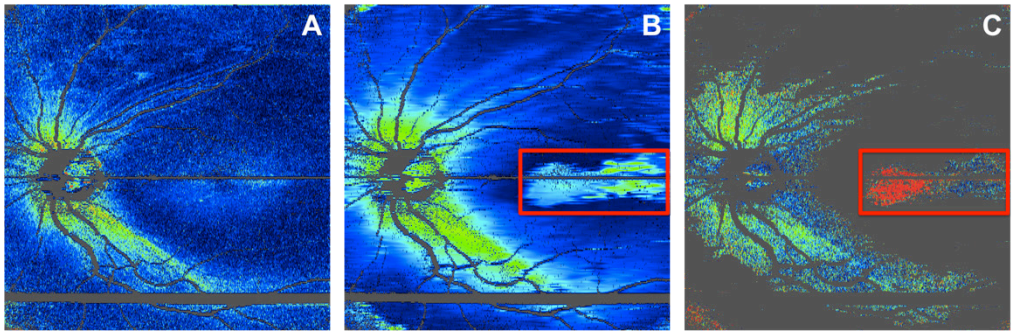

Fig. 5. RNFL retardation (a), thickness (B) and birefringence (C) en face map obtained from a glaucoma suspect patient. Color scaling is the same as in Fig. 3 and Fig. 4. Areas with low signal quality are displayed in gray. Red rectangle in B and C indicates an artifact due to incorrect segmentation of the posterior border of the RNFL.

#171147 - $15.00 USD Received 21 Jun 2012; revised 24 Sep 2012; accepted 1 Oct 2012; published 3 Oct 2012

bundle defects in the superior region. Nevertheless residual small nerve fiber bundles are still visible. The thickness map shows a decreased RNFL thickness in the superior region compared to the inferior part. Due to this decreased RNFL thickness the birefringence could not be calculated accurately in the superior region.

These images nicely show the advantage of large-field PS-OCT imaging for glaucoma diagnosis. Commercial SLP images only cover a relatively small area around the optic nerve head and hence hinder the detection of nerve fiber bundle defects located far away from the optic disc.

4.2. RPE related retinal diseases

Figure 6 shows a measurement result obtained from a patient with a large PED. Figure 6(B) shows the RPE elevation map (color scale range 0-1.2 mm). In order to calculate the elevation of this PED we used our RPE elevation map algorithm and changed the setting of the fit that estimates the normal RPE position (Savitzky–Golay filter length: 300 A-scans, polynomial order: 3). The B-scan presented in Fig. 6(C) nicely shows the advantage of the low sensitivity decay with depth of the new PS-OCT system. Although the zero delay line is located anterior to the retina (on top of the image) and the size of the PED spans almost half of the available imaging range, the new PS-OCT system is capable to image the retina without a substantial reduction of image quality.

Media 1 shows a 3D volume rendering of the intensity values in gray scale with the RPE layer colored in red. Media 2 shows the same volume rendering of the red RPE without the overlaying tissue.

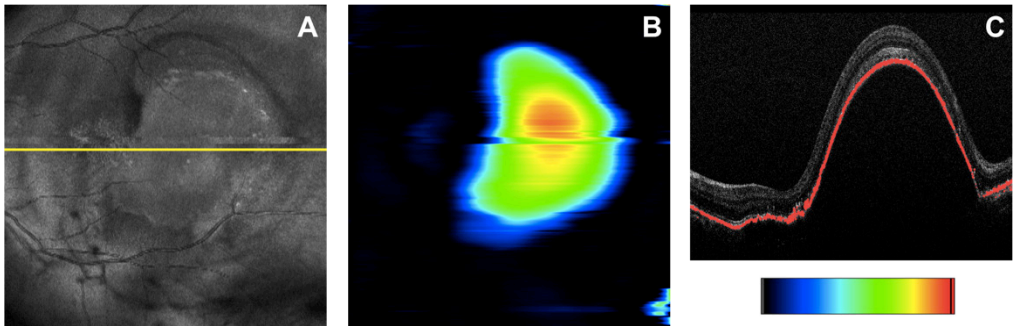

Fig. 6. PS-OCT measurement result in a patient with a large PED. (A) Pseudo SLO image. Yellow line indicates the position of the intensity B-scan overlaid with the segmented RPE in red. (B) RPE elevation map (color scale 0-1.2 mm). Media 1 shows a 3D volume rendering of the intensity values with the RPE colored in red. Media 2 shows the same volume rendering of the RPE layer in red without the overlaying tissue.

A PS-OCT measurement result obtained from a patient with drusen and GA is presented in Fig. 7. The atrophic area in the fovea region can be clearly observed in the autofluorescence image (Fig. 7(F)) and in the depolarizing material thickness map (Fig. 7(E)). Drusen, which are present superior to the GA, appear to be more pronounced and easier to distinguish in the PS-OCT image. The residual bright spots in the center of the GA that can be seen in the depolarizing material thickness map (Fig. 7(E)), mainly originate from depolarizing material in the choroid.

Figure 7 shows a typical example for an AMD related atrophic area, where only residual depolarizing material in the choroid can be observed. In contrast, Fig. 8 shows a measurement result from a patient with Stargardt's disease. Again the autofluorescence image (Fig. 8(F)) shows an atrophic zone in the fovea region. In contrast to the GA in Fig. 7, the choroid contains significantly more depolarizing material, as can be seen from the depolarizing material thickness map (Fig. 8(E)), the RPE segmentation B-scan (Fig. 8(C)) and from the DOPU image (Fig. 8(D)). The striking difference in the appearance of the two different cases

#171147 - $15.00 USD Received 21 Jun 2012; revised 24 Sep 2012; accepted 1 Oct 2012; published 3 Oct 2012

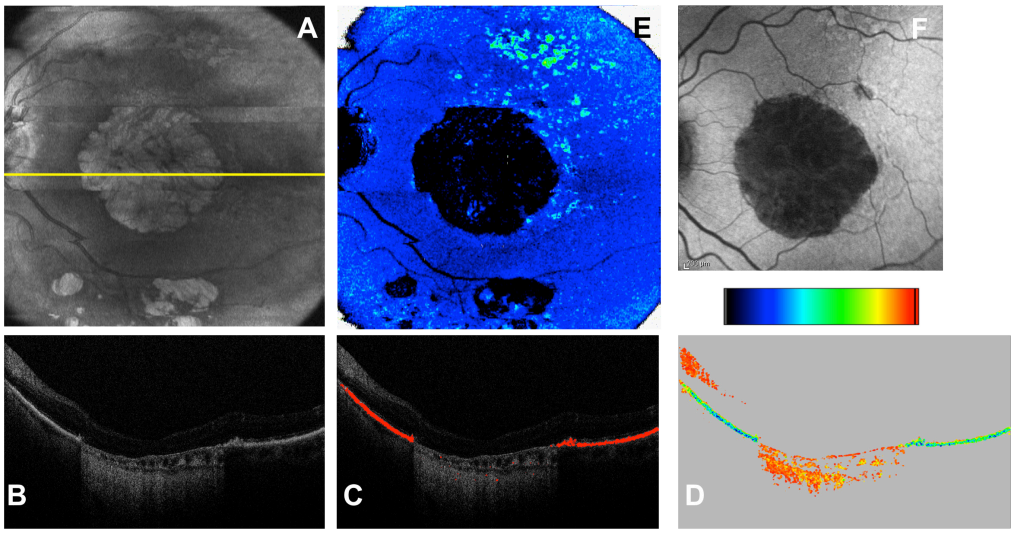

Fig. 7. PS-OCT measurement result from a patient with GA and drusen. (A) Pseudo SLO image; yellow line indicates the position of the intensity (B). (C) RPE segmentation B-scan and (D) DOPU image. (E) Depolarizing material thickness map (color scale 0-160 µm). (F) Corresponding autofluorescence image.

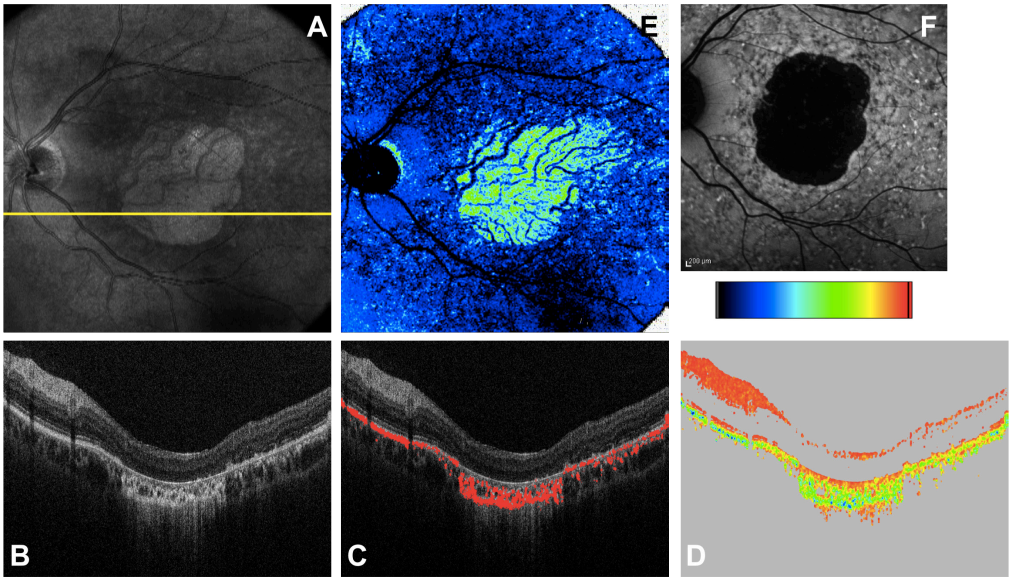

Fig. 8. PS-OCT measurement result from a patient with Stargardt's disease (pathologic mutations in the ABCA4 gene). (A) Pseudo SLO image; yellow line indicates the position of the intensity. (B). (C) RPE segmentation B-scan and (D) DOPU image. (E) Depolarizing material thickness map (color scale 0–160 µm). (F) Corresponding autofluorescence image.

of atrophies is only visible in the PS-OCT map, the autofluorescence images look very similar.

An exemplary measurement result obtained from a patient with albinism is presented in Fig. 9. The DOPU image clearly shows the reduced depolarization effect in the RPE (Fig. 9(C)) compared to a normal healthy subject (Fig. 2(E)). The depolarizing material thickness map (Fig. 9(E)) clearly reveals the reduced amount of depolarizing material within the retina compared to a healthy subject (Fig. 2(K)). This finding supports our hypothesis that the depolarizing effect of the RPE is due to multiple scattering of the imaging light caused by

#171147 - $15.00 USD Received 21 Jun 2012; revised 24 Sep 2012; accepted 1 Oct 2012; published 3 Oct 2012

melanin granules. The reduced pigmentation of the RPE in albino patients further enables a deeper penetration into the choroid. Therefore choroidal vasculature becomes visible in the pseudo SLO image (Fig. 9(A)). Noticeable is also the magnified image (zoom in) of the intensity B-scan (Fig. 9(B)). Due to the reduced multiple scattering within the RPE, an additional layer bellow the RPE can be visualized that might correspond to Bruch's membrane. This effect cannot be observed in healthy subjects (see Fig. 2(B)).

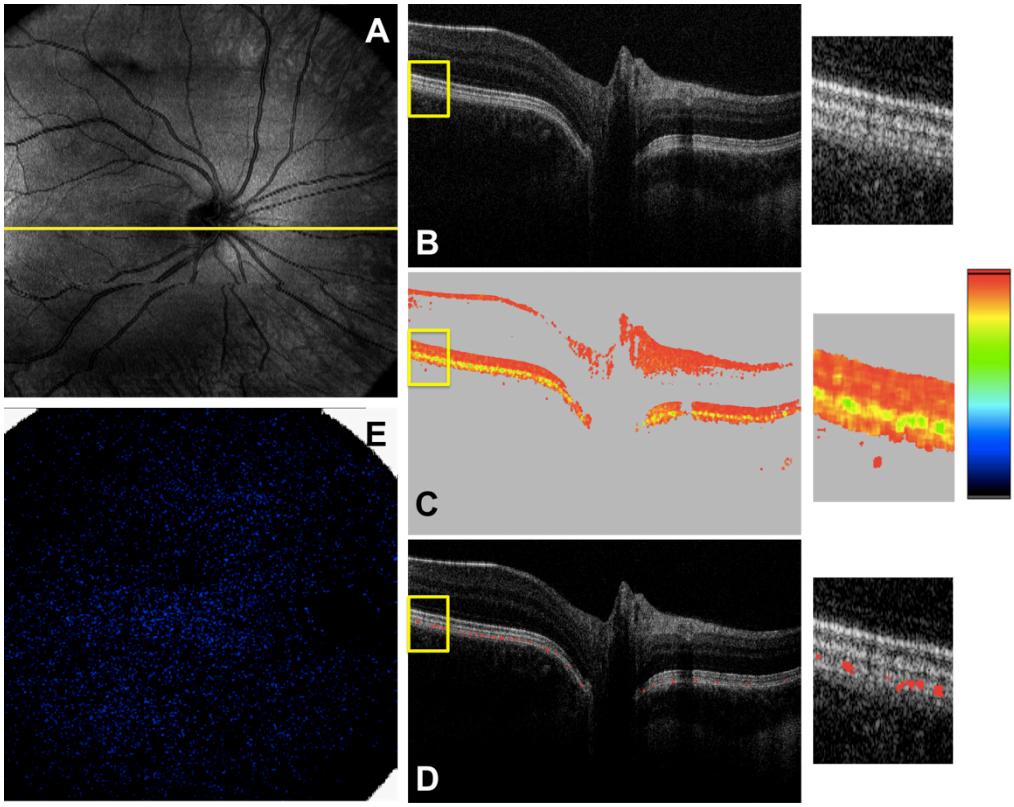

Fig. 9. PS-OCT measurement results from a patient with albinism. (A) Pseudo SLO image; yellow line marks the position of the exemplary intensity (B). (C) DOPU and (D) RPE segmentation B-scans . The yellow boxes in (B)-(D) mark the position of the magnified areas on the right. (E) Depolarizing material thickness map (color scale 0-100 µm).

5. Discussion

The presented data demonstrates the good performance of the new PS-OCT system. Due to the higher imaging speed, a denser sampling over a larger scan field is possible. These properties considerably increase the explanatory power of the recorded images.

We have presented RNFL retardation, thickness and birefringence en face maps that reveal very small details that could not be observed in previous studies with PS-OCT [25]. Compared to SLP and intensity based OCT, PS-OCT has the advantage that RNFL retardation, thickness and birefringence can be measured simultaneously but independently. This makes PS-OCT more robust against possible errors e.g. registration errors or motion artifacts that might occur between separate measurements. All three quantities might be an early sign of glaucoma [31–33]. Therefore PS-OCT might become a valuable imaging tool for future glaucoma diagnostics.

One limitation of the new PS-OCT is that the RNFL birefringence could not be measured accurately in cases where the RNFL thickness was below 60 µm. In these areas, the significance of the calculated birefringence values is limited due to the limited amount of

#171147 - $15.00 USD Received 21 Jun 2012; revised 24 Sep 2012; accepted 1 Oct 2012; published 3 Oct 2012

independent data points. One could reduce this problem by using a light source with a broader spectrum and hence a better axial resolution [20].

The large field of view RNFL retardation, thickness and birefringence maps presented here for the first time allow us to visualize the distribution of nerve fiber bundles originating from the optic nerve head and to evaluate these along the larger blood vessels within the retina. In contrast commercially available SLP images covers only a small area around the optic disc, which prevents the detection of nerve fiber bundle defects in the periphery. Further studies to investigate potential advantages of this feature are planned.

Previously, it was already shown that PS-OCT is a reliable method for measuring the number and size of drusen and the area of GA [17,34]. The new PS-OCT system, presented in this work, offers several advantages compared to previous PS-OCT systems. The high imaging speed enables the acquisition of large field of view images with high sampling density. The large-field images are especially desirable in patients with large GA. From the results presented in Fig. 7 one can see that, in addition to the large GA in the fovea region, numerous drusen are located superior to the fovea and also small GA are present inferior. This important information might be missed if imaging systems with smaller scan fields are used. Large-field scanning is also desirable for follow-up studies in patients where the size of the GA is increasing. The large-field images are also useful for imaging patients with drusen. First of all, the number and size of drusen can be monitored over a larger area within the retina. Secondly, follow-up studies are improved because an increase in the number of drusen can be monitored easily.

Another important feature of the new PS-OCT system is the low sensitivity decay with depth. This property makes it easier for clinicians to handle the system and it enables the acquisition of pathologies with large depth extensions such as the one presented in Fig. 6.

PS-OCT is not only a valuable tool for imaging patients with glaucoma and AMD but it also gives novel insights into the pathologies of several diseases. By comparing the imaging results of healthy volunteers with the one from the albino patient it is obvious that the depolarizing effect of the RPE, which can be observed in healthy eyes, is greatly reduced in albinism. This finding supports our hypothesis that melanin granules are the main cause for the depolarization effect of the RPE. On the other hand the results obtained from a patient with Stargardt's disease (presented in Fig. 8) show a strong depolarization effect in the choroid. This effect is usually not observed in patients with GA secondary to AMD. Up to now it is unclear why the choroid of this patient shows this strong depolarizing effect. Possible explanations could be that melanin granules or pigment-loaded macrophages have migrated into the choroid. Whether or not this finding provides any clinically relevant information, it might provide valuable insights for the future understanding of different diseases. This information cannot be retrieved from conventional intensity based OCT.

6. Conclusion

In this paper we have presented a novel high-speed large-field PS-OCT system. Several healthy volunteers and patients with various diseases have been imaged. The measurement results demonstrate the good performance of the system. We have shown that this new PS-OCT system is capable to combine the imaging modalities of intensity based OCT and SLP into one single instrument. Furthermore, the new PS-OCT system is capable of providing specific information on the RPE layer as autofluorescence imaging. In addition, PS-OCT provides interesting new tissue specific information in patients with different pathologies. Therefore PS-OCT might become a valuable tool for several clinical applications.

#171147 - $15.00 USD Received 21 Jun 2012; revised 24 Sep 2012; accepted 1 Oct 2012; published 3 Oct 2012